Chemical Reduction of Individual Graphene Oxide Sheets as Revealed by Electrostatic Force Microscopy

Dhaval D. Kulkarni,[†] Songkil Kim,[‡] Marius Chyasnavichyus,[†] Kesong Hu,[†] Andrei G. Fedorov,[‡] and Vladimir V. Tsukruk*,[†]

[†]School of Materials Science and Engineering and [‡]George W. Woodruff School of Mechanical Engineering, Georgia Institute of Technology, Atlanta, Georgia 30332, United States

Ⓢ *Supporting Information*

ABSTRACT: We report continuous monitoring of heterogeneously distributed oxygenated functionalities on the entire surface of the individual graphene oxide flake during the chemical reduction process. The charge densities over the surface with mixed oxidized and graphitic domains were observed for the same flake after a step-by-step chemical reduction process using electrostatic force microscopy. Quantitative analysis revealed heavily oxidized nanoscale domains (50−100 nm across) on the graphene oxide surface and a complex reduction mechanism involving leaching of sharp oxidized asperities from the surface followed by gradual thinning and formation of uniformly mixed oxidized and graphitic domains across the entire flake.

The properties of graphene materials rely on the surface functionalities and structural integrity of the sp²-carbon lattice, which can be significantly impacted by defects in the structure in the course of physical and chemical treatment. Tuning the properties of graphene is important for fabrication of "graphene papers", electronic devices, and graphene nanocomposites.[1−4] High-yield production of graphene is achieved via reduction of graphene oxide, which can be viewed as graphitic sheets with surface functionalities, such as epoxide and hydroxyl species.[5,6] The surface of graphene oxide flakes is suggested to be composed of random oxidized and graphitic domains.[7,8] Thermal or chemical reduction of graphene oxide results in partial removal of oxidized defects and dramatic increases in the electrical conductivity by 4−5 orders of magnitude to 1−10 S/m (although still well below that of the ideal graphenes because of a defective microstructure) that can be explored in design of conductive and flexible graphene-based materials.[9−11]

The average composition and chemical structure of graphene oxide materials can be verified using spectroscopic techniques such as FTIR, Raman, and X-ray photoelectron spectroscopy (XPS). Local defects under high vacuum are observed with Transmission Electron Microscopy (TEM) and Scanning Tunneling Microscopy (STM).[9,12] Scanning probe microscopy (SPM) has been employed to study the localized distribution of defects. Among others, Kelvin probe force microscopy (KPFM) has been utilized to observe the spatial distribution of the electrical potential.[13,14] Friction Force Microscopy (FFM) identified domains on graphene differing in local friction characteristics due to the ripple distortions.[15,16] Electrostatic

Force Microscopy (EFM) has been used for mapping the charge distribution, and surface potential of graphene-based materials.[17,18] Particularly, EFM studies probed the surface potential and charge distribution in graphene films.[19] Yet, consistent probing of the distribution of oxygenated defect sites on the chemically heterogeneous graphene oxide surface in the course of chemical reduction has not been demonstrated to date.

In this work, we report direct monitoring of the surface charge distribution of the same individual graphene oxide flake in the course of its stepwise chemical reduction using EFM technique. This EFM monitoring revealed that the oxidized nanoscale domains are reduced by leaching out the oxidized sites accompanied by pronounced thinning of the graphene oxide flakes and mixed defective/graphitic surface composition of conductive flakes.

Graphene oxide flakes were characterized on silicon wafers with Raman, XPS, AFM, and EFM (Figure 1). The XPS shows all the expected peaks corresponding to the silicon oxide substrate and graphene oxide (Figure 1). The C 1s spectra can be deconvoluted into three peaks corresponding to the sp² domains (C=C with a binding energy of 284.6 eV) and the oxidized sp³ domains (C−O with binding energy of 286.6 eV and O=C−
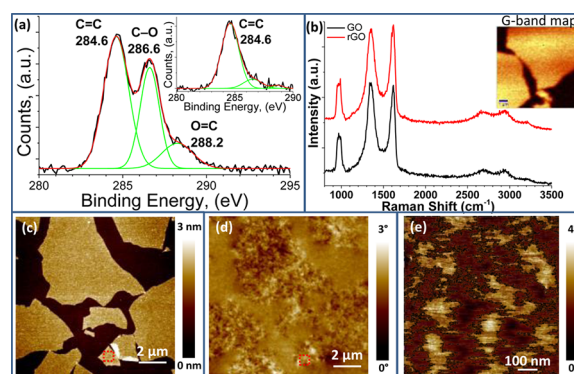
Figure 1. Graphene oxide characterization: (a) C 1s XPS spectra of graphene oxide before and after (inset, 240 s) reduction, (b) the Raman spectra before (GO) and after (rGO) reduction (inset: Raman map of G-band intensity of individual GO flakes), (c) AFM topography, (d) EFM-phase image at tip bias of +5 V and 50 nm lift height, and (e) high resolution EFM-phase image at tip bias of +5 V and 20 nm lift height. Box in (c) and (d) corresponds to the area (e).

OH with binding energy of 288.2 eV) (Figure 1a).[20] The ratio of areas under the peaks suggests that $69 \pm 5\%$ of the graphene oxide surface is oxidized with a C/O ratio of 2.1:1. The Raman map obtained by recording the intensity of the G-band between 1500 and 1650 cm^{-1} confirms presence of defects but could not resolve the spatial chemical distribution because of diffraction-limited resolution (Figure 1b, Table SI1). A uniform intensity distribution of the G- and D-band was observed over the surface of all flakes, suggesting the dominant presence of monolayer oxidized flakes. Such a highly defective microstructure is very different from idealized graphene monolayers, which show sharp Raman bands as discussed by Ruoff et al.[21]

AFM topography images further confirm the presence of mostly monolayer graphene oxide flakes several micrometers across with a thickness of 0.87 ± 0.09 nm and an RMS roughness of 0.18 nm (500 nm × 500 nm surface areas) similar to that of the supporting silicon oxide surface (0.17 nm) (Figure 1c).[22] Raman spectra of reduced graphene oxide flakes show only modest changes in peak appearance with a slightly reduced peak width and decrease in the D/G ratio (Figure 1b, Table S1). This result indicates a decrease in defect level and mixed domain distribution but is far from ideal graphene monolayers.[21] Indeed, XPS shows a dramatic reduction of oxidized bond content (Figure 1a) followed by the formation of C−N bonds at an extended reduction time (Figure S2b), confirming an effective reduction process.[10,20,21]

EFM imaging performed under ambient conditions also showed surface uniformity over the graphene oxide flake which can be attributed to water layers commonly present during ambient AFM scanning, thereby screening the surface chemical heterogeneities.[23,24] However, removing a thin water surface layer by performing the measurements under reduced humidity conditions (R.H. <2%) clearly showed nonuniform EFM characteristics on the surface of graphene oxide (Figure 1d, e). It is worth noting that ambient contaminants are inevitably present during EFM scanning even under reduced humidity conditions (dry nitrogen atmosphere) but the presence of these mobile dielectric molecules (usually hydrocarbons from air) would not significantly affect the surface distribution of oxidized groups as indirectly confirmed by unchanged surface wettability (Supporting Information (SI)).

Statistical analysis of the EFM-phase images (Figures 1, 2) revealed that the darker (lower phase shift) domains covered $60 \pm 15\%$ of the surface, which is close to the average surface coverage of functional groups estimated from the contact angle and XPS measurements (Figure 1 and SI). Moreover, high resolution EFM-phase images (pixel size below 1 nm) were collected at RH 2% and low lift height (for maximum sensitivity) which showed a high contrast in phase shift over the flake surface (Figure 1e). It is worth noting that the z-scale for all EFM-phase images is set to visually see the difference in contrast within the graphene oxide flake and between the graphene oxide flake and SiO$_2$ surface. Moreover, the high resolution image (Figure 1e) shows a greater contrast as compared to the low magnification image (Figure 1d) because a 20 nm lift height was used to capture the intricacies in the EFM-phase at high magnification.

As known, the changes in the phase and amplitude of an oscillating biased tip in EFM imaging are related to the changes in the electrostatic force gradient ($\partial F/\partial z$) with the shift in the phase ($\Delta\phi$) expressed as[25]

$$\sin(-\Delta\phi) = \frac{Q}{2\kappa}\frac{\partial^2 C}{\partial z^2}(V_{tip} - \varphi(x, y))^2 \qquad (1)$$
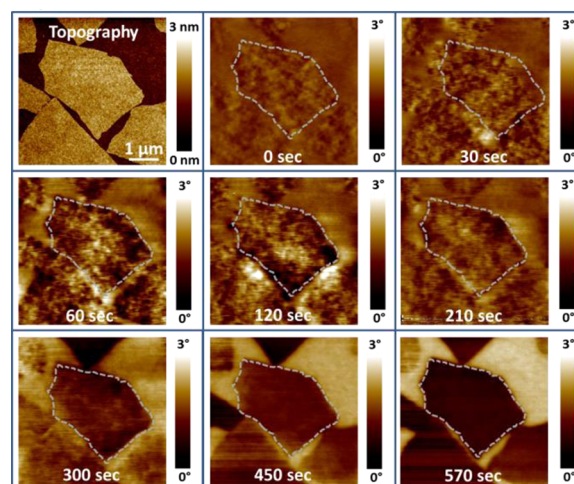
Figure 2. Topography and EFM-phase images obtained at a tip bias of +5 V and 50 nm lift height, for the same graphene oxide flake (contoured) during different chemical reaction time periods.

where C is the tip−sample capacitance, z is the tip−sample separation, V_{tip} is the voltage applied to the cantilever with respect to the grounded substrate, and $\varphi(x,y)$ is the potential distribution along the surface. If a constant bias is applied to the tip and the tip−sample distance is also maintained as constant, then the measured electrostatic force variations correspond to the changes in surface potential distribution and the specific surface potential can be derived from electrostatic force spectroscopy measurements as demonstrated in the SI. Several groups have considered the electrostatic force interaction between the tip and different graphene-based materials.[13,26,28] For instance, Salmeron et al. studied the EFM response of glass, mica, silicon, and graphite and observed that the phase shift vs tip bias followed changes in the dielectric constant of these materials.[26]

As known for graphene oxide, the surface chemical functionalities (hydroxyl, epoxy, and carboxyl) having an oxygen with a lone pair of electrons should have a lower surface potential.[27] Thus, at a positive tip bias, $V_{tip} - \varphi(x,y)$ is greater in the negatively charged oxidized areas and should result in a greater phase lag (darker areas) in the corresponding EFM-phase image. The situation is reversed on switching the tip polarity as was verified by collecting EFM-phase images of graphene oxides at the opposite tip bias (SI).[28] In contrast, the EFM-phase images of the chemically reduced graphene oxide flakes showed a uniform surface distribution of the EFM-phase shift with no reversal in the contrast at opposite tip polarities, thus, confirming the dramatic reduction of the heterogeneity of the surface composition (Figure 2).

By using this high resolution EFM-phase mapping, we monitored the stepwise chemical reduction process of graphene oxide flakes by directly monitoring the EFM-phase shift distribution at various stages of the vapor-induced chemical reaction process (Figure 2, SI). Chemical reduction is known to be caused by the surface chemical reaction with removal of oxidized surface functionalities induced by exposure to hydrazine vapor and partial restoration of sp^2 character.[29] It is important to note that, in contrast to *all previous studies*, EFM-phase imaging monitored the changes in the charge distribution for *the same flake* upon chemical reduction for different periods of time (quasi *in situ* protocol).

The most striking result is that although no significant changes in the topography were observed, the EFM-phase images clearly showed a dramatic transformation of the graphene oxide surface charges during the chemical reduction reaction (Figure 2). As soon as the flake was exposed to hydrazine vapor, the surface heterogeneity of the EFM-phase image showed an apparent change. As the chemical reaction progressed beyond the initial stage, the variations in the EFM phase decreased further and after long exposure (60−300 s) the surface of the graphene oxide flake showed a very uniform phase shift across the entire flake with no reversal of phase contrast with the change in the tip polarity (Figure 2, SI). It is worth noting that the phase difference between the flake and the substrate grows significantly with reduction time. Thus, we shifted the phase scale (keeping the same phase window) to mediate the image contrast which resulted in a change in the SiO_2 appearance (see additional images in Figure S6).

In order to analyze these transformations further, detailed quantitative analysis of the AFM and EFM images were conducted to obtain the graphene oxide flake thickness, RMS topographical microroughness, and RMS phase microroughnesses of flakes and silicon oxide surfaces calculated from the corresponding histograms (Figure 3 and SI). These measurements allowed evaluation of the changes in surface morphology and chemical functionalities caused by chemical reaction on the oxidized surface areas. First, in contrast to inconclusive results found in literature because of scattered data from bulk material analysis, we can conclude that the chemical reaction causes the gradual decrease in the flake thickness from 0.87 to 0.68 nm

(beyond the standard deviation) (Figure 3a). Such thinning reflects the partial removal of bulky oxygen-containing surface sites. Moreover, the microroughness of graphene oxide flakes remains virtually unchanged, around 0.18 nm, and identical to that for the bare silicon oxide surface (Figure 3b).

Second, the phase contrast between the graphene oxide flake and silicon oxide surface remains low and constant at the initial stage (0.2° phase shift) but increases 10-fold during the course of the chemical reaction indicating a dramatic reduction in the surface potential of the graphene oxide surface due to the elimination of oxidized sites and formation of conductive domains (Figure 3, eq 1). It is worth noting, that for bulk materials, the z-potential for reduced graphene oxide decreases to 0.002−0.007 C/m^2 from that of 0.04−0.12 C/m^2 for graphene oxide.[30] Importantly, the surface characteristics of the surrounding silicon oxide surface remain constant confirming that the chemical reaction does not affect the supporting substrate (Figure 3b). Finally, the most important reflection of the increasing surface uniformity is the gradual decrease in the RMS phase of the graphene oxide surface by almost 3-fold, from 0.17° to 0.07° (Figure 3b). Such a continuous decrease reflects the dramatic reduction of the surface potential heterogeneity of the graphene oxide surface to values common for relatively uniform silicon oxide surface layers.[22]

By analyzing the corresponding changes in the surface characteristics discussed above, we can suggest a general picture of the chemical reduction as caused by the vapor chemical reduction process of graphene oxide surfaces. First, we suggest that the initial stage of the chemical reaction (~30% of total reaction time) results in a very modest variation of the flake thickness and microroughness due to the selective chemical reduction of the "weakest" surface chemical sites of, for instance, defective chemical bonds and those located at sharp asperities, which can be easily attacked by hydrazine. At a later stage of the chemical reduction, the hydrazine slowly diffuses into surface domains with a high concentration of oxidized sites and underneath the graphene oxide flakes and reduces the oxygenated functionalities across the whole flake surface by leaching out oxygenated components and forming C−N bonds at later stages (Figure S2b). The effective thickness of the flakes reduces to 0.67 nm which is close to the theoretical values obtained for reduced graphene materials with a low concentration of defects (2−5%), in contrast to pristine graphene materials.[31] As a result of this reaction, the overall charge density reduces dramatically and the flake conductivity increases manifold.

In order to quantify the surface charge distribution from EFM images and its variation in the course of the chemical reaction, associated with the surface potential, the tip−graphene oxide surface can be idealistically approximated as a parallel plate capacitor with the adsorbed ultrathin water film as the dielectric layer. Thus, the surface potential corresponds to the potential across the capacitor system, and the surface charge density on the plates can be calculated using[28]

$$\frac{q}{A} = \frac{\epsilon_r \varphi(x, y)}{d} \tag{2}$$

where q/A is the surface charge density, ϵ_r is the relative permittivity of the medium between the plates (water, $\epsilon_r = 80$), $\varphi(x,y)$ is the surface potential, and d is the separation which is taken as the thickness of the water layer ($d \approx 0.3\ nm$).

From this relationship, the localized charge densities in the brightest and darkest areas in the EFM phase image of the graphene oxide surface were calculated to be 0.06 and 1.0 C/m^2,
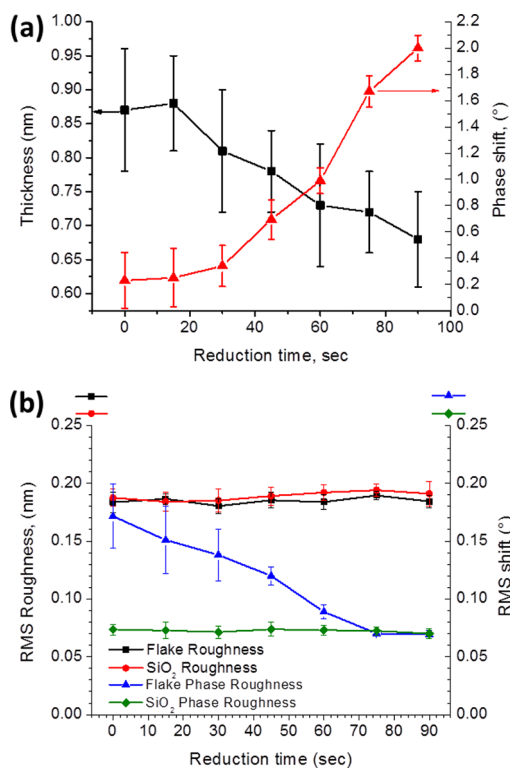
Figure 3. (a) Thickness of the graphene oxide sheet and EFM-phase shift between flake and silicon oxide at different reduction times. (b) RMS microroughness and phase shift over the graphene oxide and surrounding silicon oxide surface at different chemical reduction times. All values were calculated over a 500 nm × 500 nm surface region from the high-resolution AFM and EFM images.

6548

dx.doi.org/10.1021/ja5005416 | J. Am. Chem. Soc. 2014, 136, 6546−6549

respectively. The mapping of the local variation of chemical composition can be restored from pixel-by-pixel EFM spectroscopy which allows quantification of the local chemical composition distribution (see SI). With the assumption that the oxygenated groups contain 1 oxygen atom and the benzene ring in the graphene lattice contains effectively 2 carbon atoms (each carbon is shared by 3 neighboring rings), the C/O ratio within the heavily oxygenated domains was estimated to be 2.4:1 based on the estimated surface charge values. The values of C/O were found to be close to the values obtained from XPS (Figure 1a). On the other hand, the least oxygenated domains should contain 1 oxygen atom per 40 carbon atoms (only 5% of benzene rings with defects) after complete transformation.

At the final stages of the chemical reduction, much thinner graphene flakes with the majority of the oxygenated sites removed showed a very uniform surface potential distribution that corresponds to mixed defective and graphitic regions with higher electrical conductivity (up to 10 S/m according to literature)[9,21] (Figure 2). Moreover, the EFM-phase contrast between the reduced graphene flake and surrounding silicon substrate increases dramatically, by an order of magnitude, to 2.1°, as compared to the initial difference before the chemical reaction (~0.20°) (Figure 3). We suggest that such a high contrast could be due to the very different properties of conductive graphene flake with high surface charge mobility, supported on a dielectric silicon oxide layer and a semi-conducting silicon substrate with low charge mobility. The unchanged topographical nonuniformities (microroughness values) during chemical reduction can be related to the characteristic conformal nature of flexible graphene flakes as determined by the supporting silicon oxide that limits the ability to monitor small changes (Figure 3b).

In conclusion, we demonstrated the applicability of EFM mapping for directly monitoring the chemical transformation of graphene oxide sheets from a highly heterogeneous state with a random distribution of aggregated oxygenated surface functionalities and graphitic domains 50–100 nm across to a uniform mixture of fine domains. Such a transformation resulted in the overall conductivity of reduced graphene sheets in the course of the chemical reduction process. It is critical that such high resolution spatial imaging can be obtained in a nondestructive way for individual flakes with no special preparation of the supporting substrate, potentially *in situ* and directly on an electronic device, which makes the approach elaborated here extremely important for designing graphene-based flexible electronic materials and electronic devices.

ASSOCIATED CONTENT

Ⓢ Supporting Information

Experimental procedures and analysis. This material is available free of charge via the Internet at http://pubs.acs.org.

AUTHOR INFORMATION

Corresponding Author

vladimir@mse.gatech.edu

Notes

The authors declare no competing financial interest.

ACKNOWLEDGMENTS

REFERENCES

(1) Castro Neto, A. H.; Guinea, F.; Peres, N. M. R.; Novoselov, K. S.; Geim, A. K. *Rev. Mod. Phys.* **2009**, *81*, 109.

(2) Banhart, F.; Kotakoski, J.; Krasheninnikov, A. V. *ACS Nano* **2010**, *5*, 26.

(3) Hu, K.; Kulkarni, D. D.; Choi, I.; Tsukruk, V. V. *Prog. Polym. Sci.* **2014**, DOI: 10.1016/j.progpolymsci.2014.03.001.

(4) Xia, F.; Farmer, D. B.; Lin, Y. M.; Avouris, P. *Nano Lett.* **2010**, *10*, 715.

(5) Hummers, W. S.; Offeman, R. E. *J. Am. Chem. Soc.* **1958**, *80*, 1339.

(6) Dimiev, A.; Kosynkin, D. V.; Alemany, L. B.; Chaguine, P.; Tour, J. M. *J. Am. Chem. Soc.* **2012**, *134*, 2815.

(7) He, H.; Riedl, T.; Lerf, A.; Klinowski, J. *J. Phys. Chem.* **1996**, *100*, 19954.

(8) He, H.; Klinowski, J.; Forster, M.; Lerf, A. *Chem. Phys. Lett.* **1998**, *287*, 53.

(9) Gomez-Navarro, C.; Weitz, R. T.; Bittner, A. M.; Scolari, M.; Mews, A.; Burghard, M.; Kern, K. *Nano Lett.* **2007**, *7*, 3499.

(10) Dryer, D. R.; Park, S.; Bielawski, C.; Ruoff, R. S. *Chem. Soc. Rev.* **2009**, *39*, 228.

(11) Hu, K.; Tolentino, L. S.; Kulkarni, D. D.; Ye, C.; Kumar, S.; Tsukruk, V. V. *Angew. Chem.* **2013**, *52*, 13784.

(12) Erickson, K.; Erni, R.; Lee, Z.; Alem, N.; Gannett, W.; Zettl, A. *Adv. Mater.* **2010**, *22*, 4467.

(13) Ziegler, D.; Gava, P.; Guttinger, J.; Molitor, F.; Wirtz, L.; Lazzeri, M.; Saitta, A. M.; Stemmer, A.; Mauri, F.; Stampfer, C. *Phys. Rev. B* **2011**, *83*, 235434.

(14) Datta, S. S.; Strachan, D. R.; Mele, E. J.; Johnson, A. T. *Nano Lett.* **2008**, *9*, 7.

(15) Lee, C.; Li, Q.; Kalb, W.; Liu, X. Z.; Berger, H.; Carpick, R. W.; Hone, J. *Science* **2010**, *328*, 76.

(16) Choi, J. S.; Kim, J. S.; Byun, I. S.; Lee, D. H.; Lee, M. J.; Park, B. H.; Lee, C.; Yoon, D.; Cheong, H.; Lee, K. H.; Son, Y. W.; Park, J. Y.; Salmeron, M. *Science* **2011**, *333*, 607.

(17) Bachtold, A.; Fuhrer, M. S.; Plyasunov, S.; Forero, M.; Anderson, E. H.; Zettl, A.; McEuen, P. L. *Phys. Rev. Lett.* **2000**, *84*, 6082.

(18) Jesperson, T. S.; Nygard, J. *Nano Lett.* **2005**, *5*, 1838.

(19) Burnett, T.; Yakimova, R.; Kazakova, O. *Nano Lett.* **2011**, *11*, 2324.

(20) Yang, D.; Velamakanni, A.; Bozoklu, G.; Park, S.; Stoller, M.; Piner, R. D.; Stankovich, S.; Jung, I.; Field, D. A.; Ventrice, C. A., Jr.; Ruoff, R. S. *Carbon* **2009**, *47*, 145.

(21) Stankovich, S.; Dikin, D. A.; Piner, R. D.; Kohlhaas, K. A.; Kleinhammes, A.; Jia, Y.; Wu, Y.; Nguyen, S. T.; Ruoff, R. S. *Carbon* **2007**, *47*, 1558.

(22) McConney, M. E.; Singamaneni, S.; Tsukruk, V. V. *Polymer Rev.* **2010**, *50*, 235.

(23) Domansky, S.; Leng, Y.; Williams, C. C.; Janata, J.; Petelenz, D. *Appl. Phys. Lett.* **1993**, *63*, 1513.

(24) Zhao, M.; Gu, X.; Lowther, S. E.; Park, C.; Jean, Y. C.; Nguyen, T. *Nanotechnology* **2010**, *21*, 225702.

(25) Lei, C. H.; Das, A.; Elliot, M.; Macdonald, J. E. *Nanotechnology* **2004**, *15*, 627.

(26) Hu, J.; Xiao, X.; Salmeron, M. *Appl. Phys. Lett.* **1995**, *67*, 476.

(27) Tsukruk, V. V.; Bliznyuk, V. N. *Langmuir* **1998**, *14*, 446.

(28) Dianoux, R.; Martins, F.; Marchi, F.; Alandi, C.; Comin, F.; Chevrier, J. *Phys. Rev. B* **2003**, *68*, 045403.

(29) Gao, X.; Jang, J.; Nagase, S. *J. Phys. Chem. C* **2010**, *114*, 832.

(30) Konkena, B.; Vasudevan, S. *J. Phys. Chem. Lett.* **2012**, *3*, 867.

(31) Pandey, D.; Reifenberger, R.; Piner, R. D. *Surf. Sci.* **2008**, *602*, 1607.